pp. 1–12 (2015)

Virtual blunt injury of human thorax: age-dependent response of vascular system

K. A. Beklemysheva,* A. A. Danilov *,† I. B. Petrov *†, V. Yu. Salamatova *†, Yu. V. Vassilevski *†, and A. V. Vasyukov *

Abstract — This work is the numerical study of the age-dependent responses of the vascular system under low-mass high-speed impact scenario. The grid-characteristic method on the adaptive mesh model of the human thorax is the numerical tool of the study. Due to the lack of valid vascular injury criteria, the numerical model only provides information on injury risk. The numerical simulation demonstrates that an older age changes significantly the vascular response and increases the risk of aorta injury. We focused on the aorta because its rupture is the general consequence of vehicle accidents (great mass impacts at relatively low velocity). Our numerical results are in good agreement with previous studies of great-mass low-speed blunt thorax impact.

Keywords: Grid-characteristic method, human thorax model, blunt ballistic impact, vascular injuries, age dependence.
MSC 2010: 74L15, 92C10

The study of human thoracic impact responses has attracted considerable interest. The most of the works on blunt thoracic impact describe its biomechanics in automotive area where great mass impacts at relatively low velocity. The different impact scenario occurs in several sports (hockey, solid sports ball) or with special type of non-lethal munition used as a means of individual or crowd control. This scenario implies impacts of low-mass at high-velocity. Biomechanics of such impact and injury criteria differ from those seen in automotive research [1,3]. For example, according to Bir [3], the same skeletal injuries are caused by a lower rate of compression in the case of blunt ballistic impacts than in automotive case. Thus, direct relationship between two scenarios for injury mechanisms is not clear and injury assessment criteria for blunt ballistic impact should be elaborated in its own right. In particular this is important for the design of chest protectors.

Blunt injuries of great blood vessels are general consequences of vehicle accidents: traumatic aorta rupture is the second cause of death after brain injuries [2]. In case of low-mass high-velocity impact scenario, vascular injuries is uncommon phenomenon. Vascular injuries can be asymptomatic, however, this kind of injury leads to a significant increase in mortality [9]. Rapid identification of traumatic vascular

*Moscow Institute of Physics and Technology, Dolgoprudny 141700, Russia

†Institute of Numerical Mathematics of the RAS, Moscow 119333, Russia. Corresponding author: yuri.vassilevski@gmail.com

This work was supported by the Russian Scientific Fund (grant 14-31-00024).

injuries is required for mortality reduction.

This study investigates age-dependent responses of great blood vessels in case of blunt ballistic impact. For such type of scenario, limited data on physiologically acceptable response are available [1, 3, 4]. Therefore, a mathematical model can provide information on injury risks rather than injury forecast. Moreover, the model allows us to obtain a probable region of vessel damage after blunt ballistic impact.

The dynamic responses and injuries of thoracic viscera and vessels have been studied using human cadavers, mechanical dummies and mathematical models. Many studies simulate thorax compression to predict injury risk by finite element method [21]. We use a grid-characteristic numerical method to solve the dynamic impact problem [16]. This approach takes into account specific features of hyperbolic equations and allows to achieve high accuracy for wave solutions in heterogeneous media.

The outline of the remainder of the paper is the following. In Section 2 we recall the governing equations for dynamic processes in solids and introduce the grid-characteristic method. The results of numerical experiments for dynamic problems are presented and discussed in Section 3. Section 4 collects a few closing remarks.

1. Mathematical model of dynamic processes in solids

General dynamic equations for deformable body in the Cartesian coordinate system (x_1, x_2, x_3) have the following form:

$$\rho \dot{v}_i = \sum_{j=1}^{3} \nabla_j \sigma_{ij} + f_i^{(b)} \qquad \text{in } \Omega \qquad \text{(motion equations)}$$

$$\dot{\sigma}_{ij} = \sum_{k,l=1}^{3} q_{ijkl} \dot{\varepsilon}_{kl} + F_{ij} \qquad \text{in } \Omega \qquad \text{(rheological equations)}$$

where Ω is the domain occupied by solid, ρ is the density, v_i is the ith component of the velocity $\mathbf{v}$, σ_{ij} and ε_{ij} are the components of the stress tensor σ and deformation tensor ε, respectively, $\nabla_j = \partial/\partial x_j$ is the jth component of the gradient, $f_i^{(b)}$ is the component of the body force $\mathbf{f}^{(b)}$, tensor with components q_{ijkl} determines the rheology of the medium, F_{ij} is a right-hand side that can be used to account viscoelasticity.

The initial conditions correspond to the unstressed state of rest

$$\mathbf{v}_{|t=0} = \mathbf{0}, \quad \sigma_{|t=0} = \mathbf{0} \quad \text{in } \Omega.$$

The boundary conditions are balancing the given exterior pressure $p(t)$ imposed to a boundary patch ω:

$$(\sigma \mathbf{n}, \mathbf{n}) = -p(t) \quad \text{on } \omega \tag{1.1}$$

and traction-free on the rest of the boundary

$$\sigma \mathbf{n} = \mathbf{0} \quad \text{on } \partial\Omega \setminus \omega \tag{1.2}$$

where $\mathbf{n}$ is the unit exterior normal vector to $\partial\Omega$.

Almost all living tissues have nonlinear- and anisotropic mechanical properties. Moreover, these properties of most living tissues of an individual vary significantly with age, gender, physical conditions. Experimental studies of postmortem materials only approximate properties of most human living tissues. In vivo characterization of thoracic viscera and vessels lacks for static and dynamic experiments; this being so, following other researchers we choose the basic linear material laws (1.1).

For small strains, tensor $e_{ij} = \dot{\varepsilon}_{ij}$ can be expressed in the following form:

$$e_{ij} = \frac{1}{2}(\nabla_j v_i + \nabla_i v_j). \tag{1.3}$$

Equations of motion and rheological relations (1.1) can be rewritten in a simple matrix form:

$$\frac{\partial \mathbf{u}}{\partial t} + \mathbb{A}_{x_1}\frac{\partial \mathbf{u}}{\partial x_1} + \mathbb{A}_{x_2}\frac{\partial \mathbf{u}}{\partial x_2} + \mathbb{A}_{x_3}\frac{\partial \mathbf{u}}{\partial x_3} = \mathbf{f} \tag{1.4}$$

where $\mathbf{u} = (v_1, v_2, v_3, \sigma_{11}, \sigma_{12}, \sigma_{13}, \sigma_{22}, \sigma_{23}, \sigma_{33})^T$ is the vector of variables, $\mathbf{f}$ is the right-hand side vector of the same dimension, $\mathbb{A}_{x_1}$, $\mathbb{A}_{x_2}$, $\mathbb{A}_{x_3}$ are matrices of the ninth order.

For linear elasticity, tensor components q_{ijkl} and right-hand side components F_{ij} in (1.1) have the following form:

$$q_{ijkl} = \lambda\delta_{ij}\delta_{kl} + \mu(\delta_{ik}\delta_{jl} + \delta_{il}\delta_{jk}), \qquad F_{ij} = 0 \tag{1.5}$$

where λ and μ are Lame parameters, and δ_{ij} is Kronecker symbol. In this case, since we neglect the body force components, the right-hand side of (1.4) becomes zero.

The system of hyperbolic equations (1.4) is solved numerically by the grid-characteristic method. The main idea of the method is the following. The three-dimensional system (1.4) is split by space variables. More precisely, (1.4) is replaced with three systems of one-dimensional hyperbolic equations

$$\frac{\partial \mathbf{u}}{\partial t} + \mathbb{A}_{x_i}\frac{\partial \mathbf{u}}{\partial x_i} = 0. \tag{1.6}$$

These systems are solved sequentially by fractional time steps, the solution of the previous system is used as the initial state to solve the next one. This approach allows us to simplify numerical implementation and obtain better computation performance. The approximate solution of each system of one-dimensional hyperbolic equations at the nth time step is sought as a grid function with values $\mathbf{u}_m^n$ collocated in mesh nodes and mesh mid-edges. The computational mesh is assumed to be conformal tetrahedral, and the grid function is extrapolated quadratically in each tetrahedral cell.

Matrices $\mathbb{A}_{x_1}$, $\mathbb{A}_{x_2}$, $\mathbb{A}_{x_3}$ are diagonalizable and can be represented as:

$$\mathbb{A} = \mathbb{B}^{-1}\mathbb{D}\mathbb{B}.$$

Here indices x_i are omitted for simplicity, $\mathbb{B}$ is a matrix composed from left eigenvectors $\mathbf{b}_j^T$ of matrix $\mathbb{A}$:

$$\mathbf{b}_j^T \mathbb{A} = \lambda_j \mathbf{b}_j^T, \quad \text{or} \quad \mathbb{A}^T \mathbf{b}_j = \lambda_j \mathbf{b}_j \tag{1.7}$$

while $\mathbb{D} = \mathrm{diag}\{\lambda_j\}$ is the diagonal matrix of corresponding eigenvalues.

Premultiplying (1.6) by $\mathbb{B}$, we get the system

$$\frac{\partial \mathbb{B}\mathbf{u}}{\partial t} + \mathbb{D}\frac{\partial \mathbb{B}\mathbf{u}}{\partial x_i} = 0$$

which in the Riemann invariants $\mathbf{r} = \mathbb{B}\mathbf{u}$ becomes

$$\frac{\partial \mathbf{r}}{\partial t} + \mathbb{D}\frac{\partial \mathbf{r}}{\partial x_i} = 0.$$

Thus, the original system of equations (1.6) is split into n separate equations:

$$\frac{\partial r_j}{\partial t} + \lambda_j \frac{\partial r_j}{\partial x_i} = 0 \tag{1.8}$$

and the solution for (1.6) can be composed of independent waves with propagation speeds λ_j.

Let characteristic curves Γ be defined by

$$\frac{\mathrm{d}x_i}{\mathrm{d}t} = \lambda_j. \tag{1.9}$$

Equations (1.8) along Γ take the form

$$\frac{\mathrm{d}r_j}{\mathrm{d}t} = 0 \tag{1.10}$$

and the Riemann invariants are constant along curves Γ. Therefore, their values at the $(n+1)$th time layer and at the nth time layer are the same along these curves.

The grid-characteristic method for computing $\mathbf{u}_m^{n+1}$ at point $\mathbf{x}_m^n$ performs sequentially the steps for $i = 1, 2, 3$:

1. Compute eigenvalues λ_j for the matrix $\mathbb{A} = \mathbb{A}_{x_i}$ and corresponding characteristic curve Γ_j using (1.7)–(1.9).

2. For each characteristic curve Γ_j find the point $\mathbf{x}_{j*}^n$ on intersection of Γ_j with time layer t^n.

3. Define $\mathbf{u}_{j*}^n$ in x_{j*}^n by quadratic interpolation in mesh tetrahedron containing x_{j*}^n and slope limiting as described in [16].

4. Compute the jth Riemann invariant r^n_{j*} in the point $\mathbf{x}^n_{j*}$ using the values $\mathbf{u}^n_{j*}$. This invariant is extrapolated along Γ_j to the point $\mathbf{x}^n_m$: $r^{n+1}_{jm} = r^n_{j*}$. Define $\mathbf{r}^{n+1}_m$ from components r^{n+1}_{jm}.

5. Find the values $\mathbf{u}^{n+1}_m$
$$\mathbf{u}^{n+1}_m = \mathbb{B}^{-1}\mathbf{r}^{n+1}_m.$$

Importantly, different components of vector $\mathbf{r}^{n+1}_m$ are computed in different points $\mathbf{x}^n_{j*}$.

Once the vector $\mathbf{u}^{n+1}_m$ is computed, the grid-characteristic method updates the mesh nodes:
$$\mathbf{x}^{n+1}_m = \mathbf{x}^n_m + \Delta t\,\mathbf{v}^{n+1}_m \tag{1.11}$$
and the computational mesh is Lagrangian. The positions of mesh mid-edges are recalculated by averaging the positions of the edge endpoints rather than by (1.11).

Modelling of bodies composed of materials with substantially different rheological and mechanical properties requires the accurate solution of the contact problem: wave interactions and reflections from material boundaries affect the deformations and stresses. The grid-characteristic method allows us to set contact boundary conditions explicitly. This approach gives higher precision compared to approaches with implicit treatment of contact boundaries. The conditions on a contact boundary are set in the form of relations between variables at two adjacent points on the contacting boundaries. In this paper full-adhesive conditions are used:
$$\mathbf{v} = \mathbf{v}', \qquad \sigma\mathbf{n} = \sigma'\mathbf{n}. \tag{1.12}$$
The variables with and without primes correspond to the opposite contacting surfaces.

The grid-characteristic method offers the following advantages. Impact loads cause wave process in the medium, and high accuracy methods are required for the solution of dynamic problems. The method is designed to simulate physically correct propagation of waves with high accuracy. The accurate solution of contact problems for tissues with significantly different mechanical properties allows to recover wave propagation across multiple contacts in human thorax.

2. Numerical results

We used Visible Human Project (VHP) [22] data to construct the discrete thorax model. The initial segmentation was performed for the torso region of a human body [7,8]. The torso model was truncated to the thorax region, and Table 1 presents the main organs and tissues of the thorax model. The resolution of the segmented model is 1 mm and does not resolve vessel walls. The vasculature includes the inner domain occupied by blood and is marked with the same material.

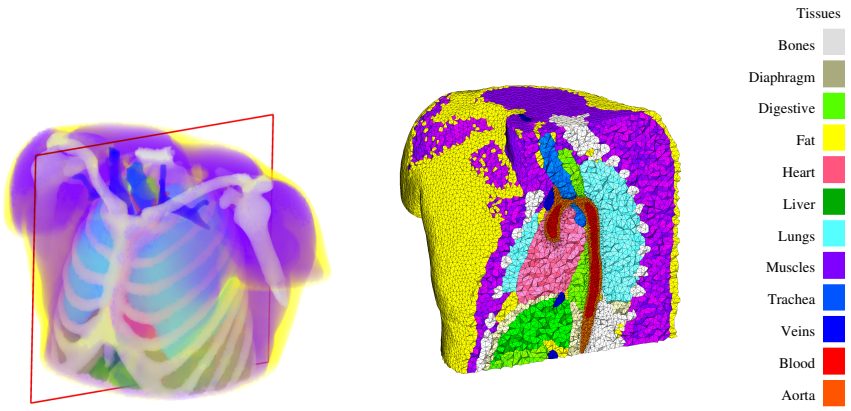

Figure 1. Anatomical thorax model: the segmented model and the saggital cross-section of the computational mesh.

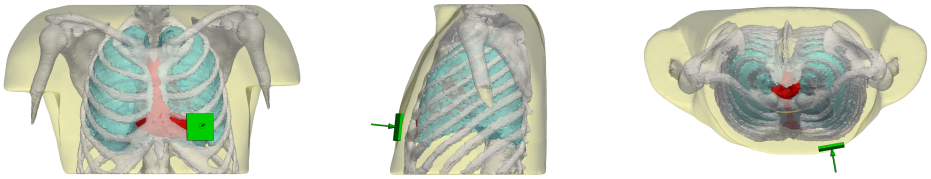

Figure 2. Thorax view, green box and arrow shows impact area and direction: coronal, saggital and transverse planes.

Accounting blood in the vasculature and the heart is important for the impact simulation; however, resolution of all great vessel walls brings about excessive mesh refinement and computational time. This work is the preliminary numerical study of vascular response, and we focus on the aorta as the most injured vessels in vehicle accidents. We consider two models of aorta: aorta is a solid structure and aorta is a vessel filled with blood. The first model extends mechanical properties of the aorta wall to the entire structure. The second model distinguishes aorta walls and blood inside aorta. The blood region in aorta is generated artificially so that the wall thickness is 2 mm. The walls were reconstructed only in the part of aorta with diameter larger than 12 mm. The other vessels are assumed homogeneous in this study.

The computational mesh is generated by the Delaunay triangulation algorithm from the CGAL-Mesh library [18]. This algorithm enables defining a specific mesh size for each model material. In order to preserve geometric features of the segmented model while keeping the number of cells feasible, we assign a smaller mesh size to blood vessels and a larger mesh size to fat and muscle tissues. An example of tetrahedral mesh adapted to blood vessels is presented in Fig. 1. The computational mesh contains 1 019 029 tetrahedra and 169 255 nodes. The mesh size ranges from 1 mm in vessels to 6 mm in fat and muscles.

All tissues and organs are considered to be elastic. Static and dynamic moduli of the soft tissue may differ significantly. Experimental studies for soft tissues are mostly performed for static loadings. In our computations, we use static moduli

Table 1. Mechanical properties of tissues and organs [11, 14, 19].

	ρ, kg/m^3	λ, MPa	μ, MPa
Fat	1000	1.0e+00	7.5e−01
Muscles	1000	3.1e+00	2.1e+00
Bones	1000	7.7e+02	1.1e+03
Lungs	600	2.9e−02	7.1e−04
Diaphragm	1000	5.8e+00	3.6e+00
Liver	1200	2.4e−01	6.1e−02
Trachea	2000	1.4e+01	3.6e+00
Oesophagus	1200	7.1e+00	1.8e+00
Heart	1000	2.4e−01	6.0e−02
Blood	1000	2.4e−01	5.0e−04
Arteries (20-year-old)	1000	6.0e+00	1.6e−01
Veins (20-year-old)	1000	1.6e+01	3.5e−01
Arteries (40-year-old)	1000	9.2e+00	1.9e−01
Veins (40-year-old)	1000	3.3e+01	6.7e−01
Arteries (60-year-old)	1000	1.9e+01	3.9e−01
Veins (60-year-old)	1000	5.6e+01	1.1e+00

presented in previous blunt thoracic impact studies [11, 14, 19]. Mechanical properties of tissues and organs are presented in Table 1. Age-dependent vessel stiffness is based on data from [5].

We simulate the direct impact to thorax as boundary condition (1.1) imposed on a small square patch ω on the thorax surface $\partial\Omega$ (see Fig. 2). The impact energy is 8.0 kJ that corresponds to the energy distributed by a bulletproof vest after a rifle shot. The rest of the thorax surface is assumed to be traction-free (1.2). We treat the external force as pressure imposed on the impact area for 134 microseconds.

In failure mechanics two stress-based criteria are conventional: the von Mises criterion and the maximum principal stress criterion. The von Mises stress σ_{mises} is defined by

$$\sigma_{\text{mises}} = \sqrt{\frac{(\sigma_1-\sigma_2)^2+(\sigma_2-\sigma_3)^2+(\sigma_3-\sigma_1)^2}{2}} \tag{2.1}$$

where $\sigma_1 \geqslant \sigma_2 \geqslant \sigma_3$ are the principal stresses.

According to the von Mises criterion, the failure occurs when von Mises stress exceeds the ultimate stress $\sigma_{u,m} > 0$:

$$\sigma_{\text{mises}} > \sigma_{u,m}. \tag{2.2}$$

According to the maximum principal stress theory, failure occurs when the maximum principal stress exceeds the value of the ultimate stress $\sigma_{u,1} > 0$ in simple tension:

$$\sigma_1 > \sigma_{u,1}. \tag{2.3}$$

The ultimate stresses $\sigma_{u,m}$, $\sigma_{u,1}$ are material constants and should be properly determined. Unfortunately, in soft tissue mechanics these constants are not well established and both failure criteria can not be used.

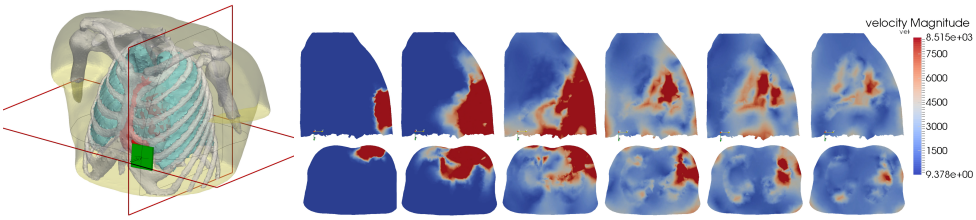

Figure 3. Velocity modulus for 8 kJ strike at different time points (18 mcs, 3.6 ms, 7.2 ms, 10.8 ms, 14.4 ms, 18 ms). On the top - a slice in the saggital plane, at the bottom - in the transverse plane; 40 years age group. The velocity unit is cm/sec.

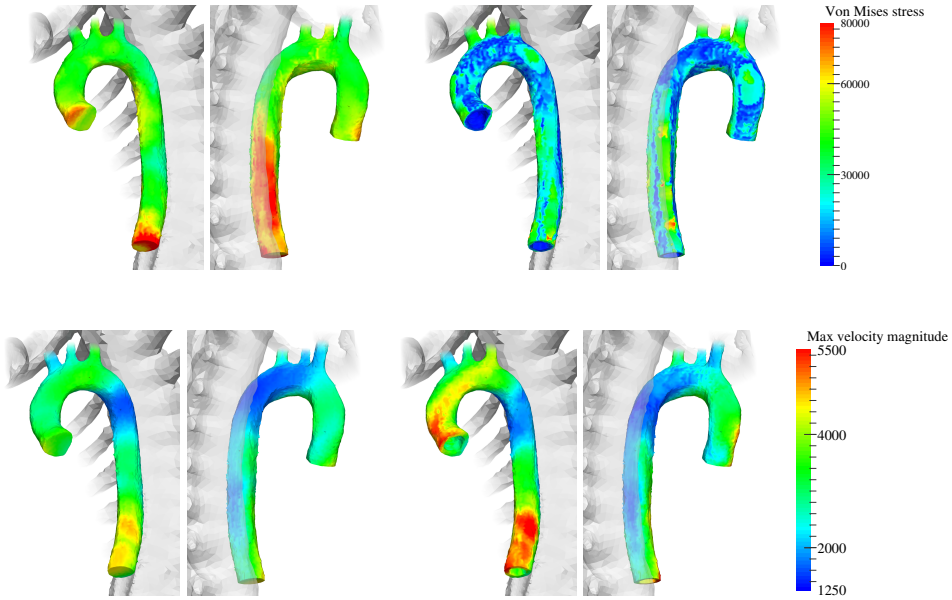

Figure 4. Comparison of aorta models for 60 years age group: maximum von Mises and maximum velocity modulus observed in simulation; two-sides views. On the left: homogeneous model (wall material occupies entire vessel); on the right: aorta filled with blood. Stress and velocity units are Pa and cm/sec, respectively.

Using grid-characteristic method we obtain distributions of stress and velocity at the nodes of the computational mesh for different age groups. The results allow us to find maximum von Mises stresses, maximum tensions and maximum velocities over the simulation time:

$$\max_{t>0} \sigma_{\text{mises}}, \quad \max_{t>0} \sigma_1, \quad \max_{t>0} |\mathbf{v}|$$

and analyze them as functions of $\mathbf{x}$.

Figure 3 presents characteristic wave patterns at different time moments. As one can see, elastic waves propagate in lungs much slower than in other organs and tissues: everywhere waves already dissipated by the time when the primary

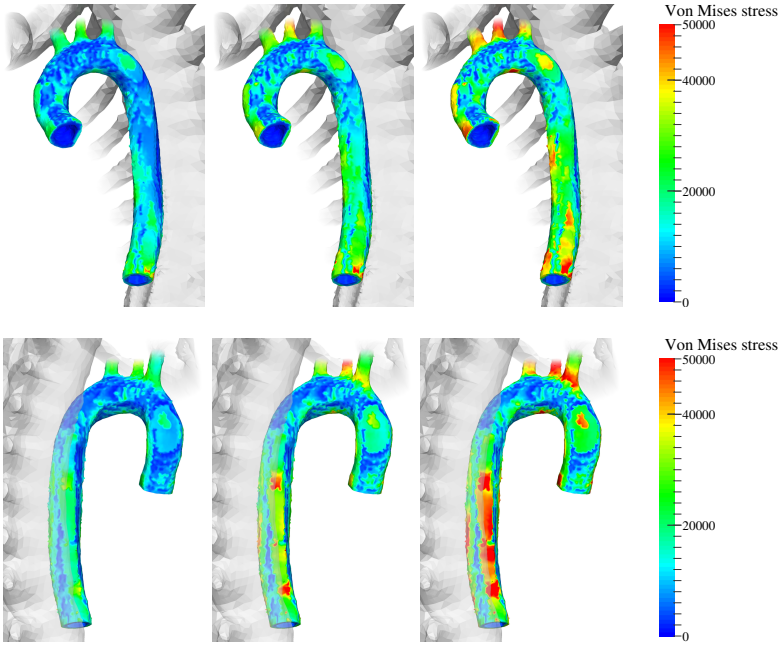

Figure 5. Aorta age-dependent response. Two-sides views for distribution of maximum von Mises stress observed in simulation: 20 years age group (left), 40 years age group (middle), 60 years age group (right). Stress unit is Pa.

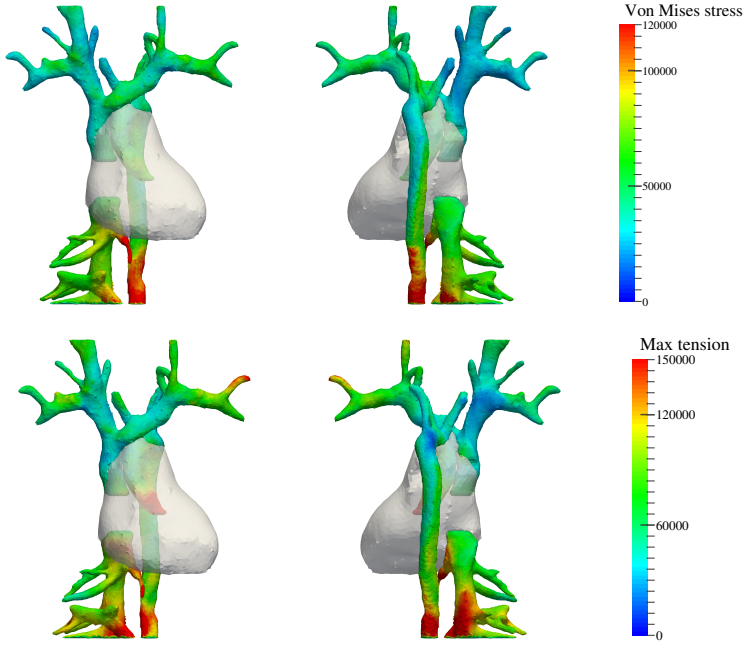

Figure 6. Distribution of the maximum von Mises stress observed in simulation (upper row) and the maximum tension observed in simulation (bottom row) for the non-tubular model of the vasculature, 60 years age group. Stress unit is Pa.

wave sweeps across the lung. The result can be related to the fact that pulmonary contusion is one of the main injuries caused by a blunt ballistic impact [3].

We compare velocity and stress distributions for different aorta elastic models (see Fig. 4). According to the simulation results, blood incorporation distresses significantly the aortic wall and changes the velocity field. In the case of the tubular aorta model, the maximum values of the von Mises stress reduce by 25% and the maximum values of the velocity magnitude increase by 20%. At the same time, the velocity and stress distributions do not differ significantly in the three major aorta branches. Such similarity is conditioned by the non-tubular representation of the branches in both aorta models because of numerical difficulties discussed above. In the following analysis we will focus on the aortic wall within the tubular aorta model.

Figure 5 presents age-dependent responses of the aortic wall. As one can see, aging leads to the increase of the maximum von Mises stress. To the best of our knowledge, no studies on the age-dependent ultimate stress $\sigma_{u,m}$ are available in the literature; however, similar research on the age-dependent dynamic tension strength [15] allows us to assume that the ultimate stress $\sigma_{u,m}$ *decreases* with aging. Therefore, the increase of the maximum von Mises stress with age implies increasing risk to injury. The maximum von Mises stress for 40 years age group is in average 50% higher than that for 20 years age group; the maximum von Mises stress for 60 year-old group is in average 30% higher than that for 40 year-old group. If we assume that $\sigma_{u,m}$ is not age-dependent (conservative assumption), the factor of safety decreases each twenty years in average by 28%. This conclusion on age dependency of the safety factor correlates with high mortality in elderly group (age above 55 years) caused by blunt traumatic thoracic aortic lacerations [6].

The regions of high von Mises stresses are in a good agreement with previous numerical results on blunt traumatic aorta rupture [17]. We can highlight three main aortic wall areas with maximum (over simulation time) value of the von Mises stress (see Fig. 5): peri-isthmus region, region of contact with bones and ascending aorta. The regions of high von Mises stresses occur for two reasons. The first one is a surface wave of high amplitude that propagates along traction-free bottom boundary of the thorax (see upper row of Fig. 3). The second reason is the full-adhesive contact of aorta with the vertebral column condition (1.12). According to clinico-pathological studies, the primary site of the aortic ruptures caused by vehicle accidents is peri-isthmus region [10,12,20], although any portion of the thoracic aorta is at risk. Therefore, the computed von Mises stress is in accordance with the numerical results and clinico-pathological studies for great-mass low-velocity impacts.

A high aortic wall tension is one of possible reasons of traumatic aortic rupture. According to our numerical results, the maximum value of tension among all ages (about 116 kPa) is far less than the failure threshold for aorta (2800 kPa [15]). Thus, in the considered impact scenario, the wall tension does not cause aortic rupture.

Non-tubular solid models of entire vasculature can be used for qualitative analysis of the thoracic impact response as well. For instance, within this model age plays the similar role and facilitates the injury. Moreover, distribution of stress for

vena cava is similar to that for the aorta (see Fig. 6). Therefore, in the scope of the considered impact scenario, vena cava, similarly to aorta, is at risk of injury. This is in agreement with findings [13].

3. Conclusions

We studied numerically the age-dependent responses of the vascular system under low-mass high-speed impact scenario. Our tool is the grid-characteristic method on the adaptive mesh model of the human thorax. This work is the preliminary study of the vascular system response for such type of impact. Due to the lack of valid vascular injury criteria the mathematical model provides only information on injury risk. We focused on the aorta because its rupture is the general consequence of vehicle accidents. Our numerical results are in good agreement with previous studies of great-mass low-speed blunt thorax impact. The risk of injury for the other vessels will be considered in the future work.

In our study we considered passive mechanical properties of soft tissues. It is well-known that elastic moduli of cardiovascular system vary during the cardiac cycle. At present stage of our research we did not take into account such variability of mechanical properties. Also, in future studies we will treat soft tissues as viscoelastic material, that is more physiologically correct.

According to our numerical model, older age changes significantly the vascular response and increases the risk of injury. Apart of traumatic vascular rupture, possible blood vessel subfailures (e.g. pseudo-aneurysm, dissection) should be examined. Severe vascular injuries may occur without vivid clinical manifestations, and the outcome of injuries is unpredictable and unfavorable. Our results indicate that the older is the person, the more demanding is early diagnosis.

References

1. A. Awoukeng Goumtcha, M. Bodo, L. Taddei, and S. Roth, From military to civil loadings: Preliminary numerical-based thorax injury criteria investigations. *Int. J. Numer. Method Biomed. Engrg.* (2015).
2. A. Belwadi, J. H. Siegel, A. Singh, J. A. Smith, K. H. Yang, and A. I. King, Finite element aortic injury reconstruction of near side lateral impacts using real world crash data. *J. Biomech. Engrg.* **134** (2012), No. 1, 011006.
3. C. A. Bir, *The evaluation of blunt ballistic impacts of the thorax.* Doctoral Thesis. Wayne State University, Detroit, 2000.
4. C. Bir, D. Viano, and A. King, Development of biomechanical response corridors of the thorax to blunt ballistic impacts. *J. Biomech.* **37** (2004), No. 1, 73–79.
5. J. Black and G. Hastings, *Handbook of Biomaterial Properties*. Springer Science & Business Media, 2013.
6. P. C. Camp Jr., F. B. Rogers, S. R. Shackford, B. J. Leavitt, R. A. Cobean, and D. E. Clark, Blunt traumatic thoracic aortic lacerations in the elderly: an analysis of outcome. *J. Trauma* **37** (1994), No. 3, 418–425.

7. A. A. Danilov, D. V. Nikolaev, S. G. Rudnev, V. Y. Salamatova, and Y. V. Vassilevski, Modelling of bioimpedance measurements: unstructured mesh application to real human anatomy. *Russ. J. Numer. Anal. Math. Modelling* **27** (2012), 431–440.

8. A. A. Danilov, V. Yu. Salamatova, and Yu. V. Vassilevski, Mesh generation and computational modelling techniques for bioimpedance measurements: an example using the VHP data. *J. Phys.: Conf. Series* **407** (2012), No. 1, 012004.

9. J. C. Eun, M. Bronsert, K. Hansen, S. L. Moulton, O. Jazaeri, M. Nehler, and J. I. Greenberg, Vascular injury is associated with increased mortality in winter sports trauma. *Ann. Vasc. Surg.* **29** (2015), No. 1, 109–113.

10. R. M. Greendyke, Traumatic rupture of aorta: special reference to automobile accidents. *Jama* **195** (1966), No. 7, 527–530.

11. E. Haug, H.-Y. Choi, S. Robin, and M. Beaugonin, Human models for crash and impact simulation. In: *Computational Models for the Human Body. Special Volume of Handbook of Numerical Analysis* (Ed. N. Ayache). Elsevier, 2004, pp. 231–452.

12. D. Katyal, B. A. McLellan, F. D. Brenneman, B. R. Boulanger, P. W. Sharkey, and J. P. Waddell, Lateral impact motor vehicle collisions: significant cause of blunt traumatic rupture of the thoracic aorta. *J. Trauma*, **42** (1997), No. 5, 769–772.

13. H. Liu, J. Chen, J. Y. Kang, X. X. Li, and I. Azhari, Finite element analysis of the dynamic response of the cardiovascular system to the blunt ballistic impact. *Computer Modelling and new Technologies* **18** (2014), No. 5, 44–49.

14. J. A. Lobuono and Y. W. Kwon, *Modelling the Biodynamical Response of the Human Thorax with Body Armor from a Bullet Impact.* Monterey, California. Naval Postgraduate School, 2001.

15. D. Mohan and J. W. Melvin, Failure properties of passive human aortic tissue. I – uniaxial tension tests. *J. Biomech.* **15** (1982), No. 11, 887–902.

16. I. B. Petrov, A. V. Favorskaya, A. V. Shevtsov, A. V. Vasyukov, A. P. Potapov, and A. S. Ermakov, Combined grid characteristic method for the numerical solution of three dimensional dynamical elastoplastic problems. *Comp. Math. Math. Phys.* **54** (2014), No. 7, 1176–1189.

17. D. Richens, M. Field, S. Hashim, M. Neale, and C. Oakley, A finite element model of blunt traumatic aortic rupture. *Eur. J. Cardiothorac. Surg.*, **25** (2004), No. 6, 1039–1047.

18. L. Rineau and M. Yvinec, A generic software design for Delaunay refinement meshing. *Comp. Geometry* **38** (2007), 100–110.

19. J. Saadé, A.-L. Didier, P.-F. Villard, R. Buttin, J.-M. Moreau, M. Beuve, and B. Shariat, A preliminary study for a biomechanical model of the respiratory system. In: *Engineering and Computational Sciences for Medical Imaging in Oncology-ECSMIO 2010*, May 2010, Angers, France, p. 7.

20. S. Sevitt, Traumatic ruptures of the aorta: a clinico-pathological study. *Injury* **8** (1977), No. 3, 159–173.

21. K. H. Yang, J. Hu, N. A. White, A. I. King, C. C. Chou, and P. Prasad, Development of numerical models for injury biomechanics research: a review of 50 years of publications in the Stapp Car Crash Conference. *Stapp Car Crash J.* **50** (2006), 429–490.

22. The National Library of Medicine's Visible Human Project. http://www.nlm.nih.gov/research/visible.